



An Extreme Radio Fluctuation of Pulsar B1929+10

Zhengli Wang¹ , Shunshun Cao² , Jiguang Lu^{3,4} , Yulan Liu^{3,4} , Xun Shi⁵ , Jinchun Jiang³ , Enwei Liang¹ ,
Weiyang Wang⁶ , Heng Xu³ , and Renxin Xu^{2,7,8}

¹ Guangxi Key Laboratory for Relativistic Astrophysics, School of Physical Science and Technology, Guangxi University, Nanning 530004, People's Republic of China; lew@gxu.edu.cn

² Department of Astronomy, School of Physics, Peking University, Beijing 100871, People's Republic of China; r.x.xu@pku.edu.cn

³ National Astronomical Observatories, Chinese Academy of Sciences, Beijing 100012, People's Republic of China; lujig@nao.cas.cn

⁴ Guizhou Radio Astronomical Observatory, Guiyang 550025, People's Republic of China

⁵ South-Western Institute for Astronomy Research (SWIFAR), Yunnan University, Kunming 650500, People's Republic of China

⁶ School of Astronomy and Space Science, University of Chinese Academy of Sciences, Beijing 100049, People's Republic of China

⁷ State Key Laboratory of Nuclear Physics and Technology, Peking University, Beijing 100871, People's Republic of China

⁸ Kavli Institute for Astronomy and Astrophysics, Peking University, Beijing 100871, People's Republic of China

Received 2024 August 16; revised 2024 October 14; accepted 2024 October 18; published 2024 November 27

Abstract

We report the detection of an extreme flux decrease accompanied by clear dispersion measure (DM) and rotation measure (RM) variations for pulsar B1929+10 during the 110 minute radio observation with the Five-hundred-meter Aperture Spherical radio Telescope. The radio flux decreases by 2–3 orders of magnitude within a rapid timescale of about 20 minutes. Meanwhile, the variations of DM and RM are approximately 0.05 pc cm^{-3} and 0.7 rad m^{-2} , respectively. Frequency-dependent analysis of DM indicates an extremely weak chromatic DM feature, which does not notably affect the radiative behavior detected. Moreover, the pulsar timing analysis shows an additional time delay from $100 \mu\text{s}$ to $400 \mu\text{s}$ in the event. These results are speculated to be due to the eclipse and bend for the radio emission of pulsar B1929+10 by a highly dense outflow from the pulsar. This not only impacts the intrinsic radio emission feature but also affects the pulsar timing behavior. Nevertheless, a plasma lens effect lasting around 20 minutes could also be responsible for the event.

Unified Astronomy Thesaurus concepts: [Radio pulsars \(1353\)](#); [Interstellar medium \(847\)](#); [Plasma astrophysics \(1261\)](#)

1. Introduction

The interstellar medium (ISM) can modulate the radio emission of pulsars in various ways, such as the electron density fluctuations (inducing scintillation) and the scattering that can influence the detection of the radio pulsars (e.g., R. S. Foster & J. M. Cordes 1990; J. M. Cordes & R. M. Shannon 2010). These effects also influence the understanding of the intrinsic radio emission of the pulsars. Besides, some regions with higher electron density can cause plasma lensing phenomena (e.g., R. L. Fiedler et al. 1987; K. W. Bannister et al. 2016). The origin of these events is usually interpreted as extreme scattering events (ESEs). Theories of the plasma lensing effects based on the two different density profiles, such as Gaussian and power-law cases, have been investigated in previous works (e.g., J. M. Cordes et al. 2017; M. T. Lam et al. 2020; X. Er & S. Mao 2022).

Previous observations of the plasma lensing events due to the ESEs indicate that the plasma lensing events that impact the amplitude of the flux density of the targeted radio source usually have about a 50% decrease, and a few events reach a 10^{-1} decrease. They usually last for long durations, ranging from several hours to days, and even several weeks to months (e.g., R. L. Fiedler et al. 1987; I. Cognard et al. 1993; G. Cimò et al. 2002; K. W. Bannister et al. 2016). A short timescale of the plasma lensing event was observed by R. Main et al. (2018) in an eclipsing binary system. Due to this plasma lensing event, the observed radio flux is enhanced by factors ranging from 70 to 80 at specific frequencies.

In this work, we report an extreme radio fluctuation of pulsar B1929+10 that includes a decrease down to 10^{-3} in the pulsar's flux density that lasted for about 20 minutes during our 110 minute observation. The short duration and the low flux are unusual compared to previously reported plasma lensing events (due to the ESEs or in an eclipsing binary system). The variations in pulsar B1929+10 could help us to constrain the local region around this pulsar and the environment along the line of sight (LOS), but it is challenging to interpret their origins. These variations are important for studying the ISM environment and understanding the intrinsic radio emission of the targeted radio sources. Meanwhile, this event yields an additional delay in pulsar timing measurement, which influences the pulse arrival times with the submicrosecond accuracy required for the detection of nanohertz-frequency gravitational waves (GWs; e.g., R. S. Foster & D. C. Backer 1990; M. Kramer et al. 2006, 2021; P. B. Demorest et al. 2013; G. Agazie et al. 2023; EPTA Collaboration et al. 2023; H. Xu et al. 2023).

Section 2 describes the 110 minute observation for pulsar B1929+10 carried out by the Five-hundred-meter Aperture Spherical radio Telescope (FAST) and data processing. In Section 3, we present the related results of this observation, while in Section 4, we discuss the outflows from the pulsar that result in the variations in pulsar B1929+10 and present other possible origins. Section 5 summarizes our main conclusions.

2. Observation and Data Processing

The normal 226 ms pulsar B1929+10 with a distance of $\sim 0.331 \text{ kpc}$ (e.g., W. F. Brisken et al. 2002; G. Hobbs et al. 2004) and both a main pulse and an interpulse (e.g., J. A. Phillips 1990; J. M. Rankin & N. Rathnasree 1997) was observed

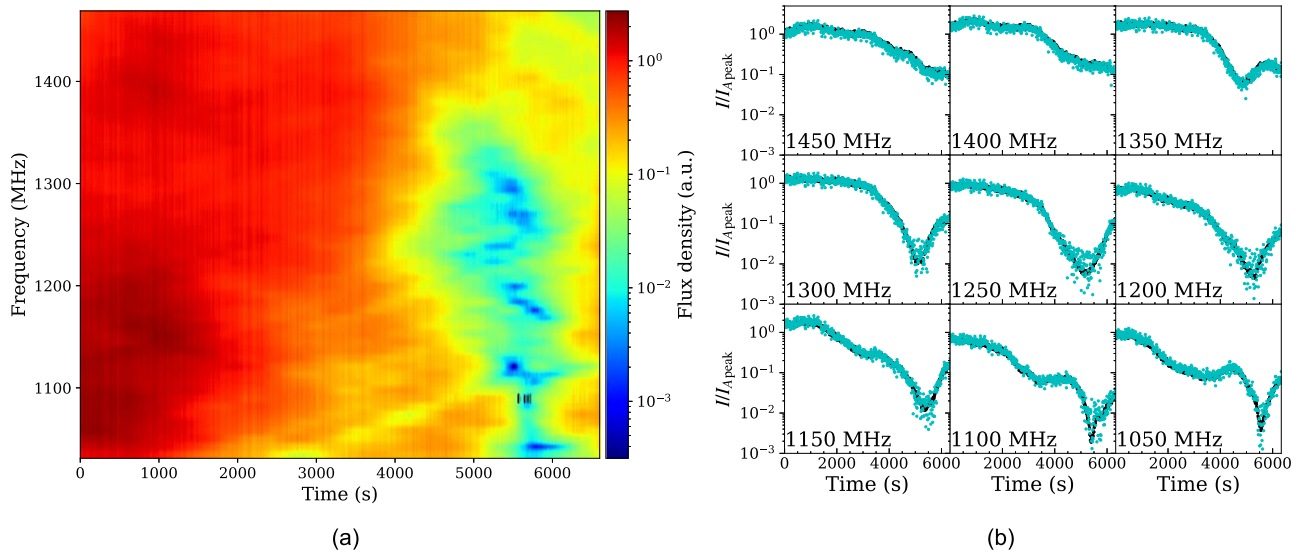


Figure 1. (a) Dynamic spectrum averaged to around 8 MHz frequency resolution for the main pulse of pulsar B1929+10. We choose an integration time of approximately 10 s (45 rotation periods) for each spectrum to minimize the impact of system noise. The flux density has been scaled with the peak radio emission of the averaged pulse. (b) To better reveal variations over the frequencies and the arrival time, we plot the observed flux densities (black dots) for the main pulse as a function of the observation time for nine narrow bands with a bandwidth of 50 MHz. Their corresponding centered frequencies are included in the lower left corner of each subpanel, while the cyan dots denote the flux density of the interpulse. The $I_{A,\text{peak}}$ represents the peak radio emission of the average pulse for the main pulse, corresponding to the peak radio emission of the interpulse of the averaged pulse. The integration time of each dot is the same as that of each spectrum.

with FAST on MJD 59904 (2022 November 21) using a 19 beam receiver system (P. Jiang et al. 2019, 2020). The observation lasts 110 minutes and is carried out in tracking mode by FAST. The raw data were recorded in the 8 bit-sampled search mode PSRFITS format (A. W. Hotan et al. 2004) with a sampling time of 49.152 μs . The frequency resolution is about 0.122 MHz, and the recorded frequency channel number is 4096. To obtain precise polarization emission features of the averaged pulse and single pulse, accurate polarization calibration signals of 30 s were injected after each observation length for the 30 minutes required in our observation. The data processing was carried out by the DSPSR software package (W. van Straten & M. Bailes 2011), and the raw data were folded with a time resolution of 0.226 ms. About 28,000 individual pulses were obtained from the entire 110 minute observation. The radio frequency interference (RFI) is mitigated by using the dynamics spectrum in the frequency time to eliminate the impact of RFI on the pulse emission of pulsar B1929+10.

3. Results

3.1. Variations in the Observed Flux Density

Pulsar B1929+10 is a bright pulsar, so the variation in its observed flux density is a probe to unravel the environment along the LOS (e.g., B. J. Rickett 1990; Y. Liu et al. 2022; S. K. Ocker et al. 2024). Figure 1 depicts the fluctuations in the observed flux density of pulsar B1929+10, showing that the flux density exhibits a distinctive and significant fluctuation. These fluctuations depend on the observing frequencies. Except for the frequencies higher than 1375 MHz, the observed flux density at other frequencies shows a significant decrease of 3 orders of magnitude. After dropping to the minimum, the observed flux density then increases, forming a “valley” structure (the blue and navy blue patches) during the range of 5000–6200 s. The timescales of the decrease and increase are almost equal, implying a symmetrical “valley” structure. The

decrease up to about 3 orders of magnitude and the maximum width of the “valley” (the timescale of the fluctuation) is detected at 1250 MHz. The observed flux density at some frequencies decreases by even more than 3 orders of magnitude (the navy blue patches). There is an increase in flux density around 3200 s at frequencies lower than 1125 MHz, forming a shallow “valley” structure (the yellow patches) from 2000 to 5000 s. The observed radio flux is reduced by a factor of about 10. Moreover, the yellow patches experience a time delay as the frequency increases.

The start of the fluctuation in the observed flux density also shows a frequency difference. The earliest variations start at 4000 s and are detected at 1250 MHz. The dramatic decrease starting at 1100 MHz is observed from 5500 s. In addition, in Figure 1(b), one can see that the arrival time of minimum flux density has a significant decrease when the frequency increases, showing a power-law function of $t = 1.36 \times 10^5 f^{-0.46}$. Here t and f are measured in units of seconds and MHz, respectively. Moreover, the observed flux densities at frequencies higher than 1375 MHz decreased but did not increase over the remaining 90 minutes of observation after the integration time of 1000 s. However, this increase is not detected in other frequencies. Another decrease of the flux density was detected at 1350 MHz after the observation of 5800 s.

3.2. Variations in Dispersion Measure and the Detection of the Chromatic Dispersion Measure

The dispersion measure (DM) in a cold, uniform, unmagnetized plasma yields a dispersive delay between different frequencies and can be described as follows (e.g., D. R. Lorimer & M. Kramer 2012; J. M. Cordes et al. 2016; Y. Men & E. Barr 2024):

$$\Delta t = \mathcal{D} \times \text{DM} \times \left(\frac{1}{f_1^2} - \frac{1}{f_2^2} \right). \quad (1)$$

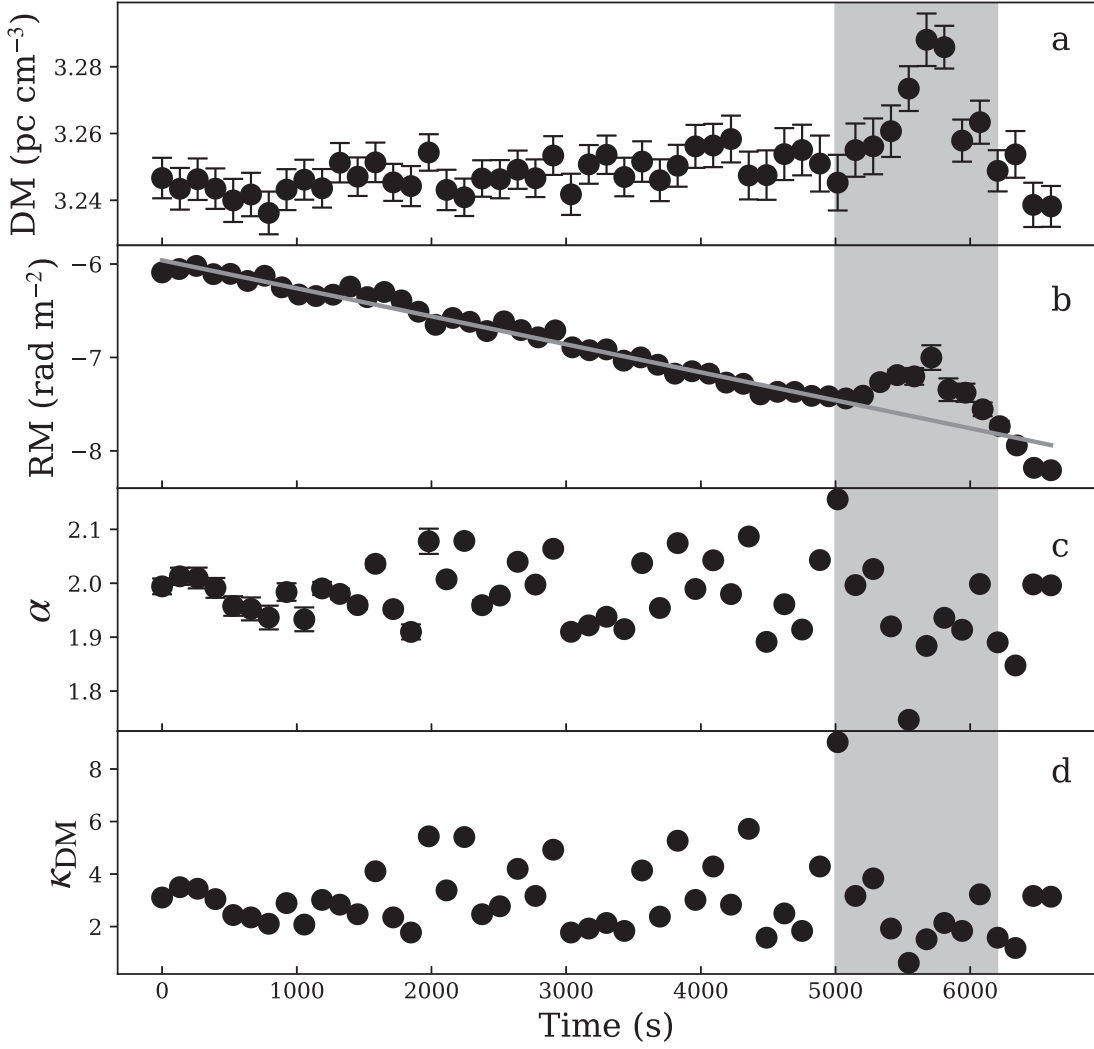


Figure 2. Variations over the entire 110 minute observation. We plot the measured DM (a), the measured RM (b), the detection of α (c), and the measured κ_{DM} (d) as a function of the observation time. Each dot corresponds to an integration of 2 minutes. To better exhibit the event, we use the vertical gray shadow to mark the region of the event.

Here, $D = \frac{e^2}{2\pi m_e c}$ corresponds to the dispersion constant, e and m_e are the charge and mass of the electron, and c is the speed of light. It is described by the relation $\text{DM} = \int n_e dl$, where n_e represents the electron number density and the integration $\int dl$ is along the LOS. The radio waves of the pulsars can be believed to be a probe that unravels the environment along the LOS. Variations in DM indicate that the electron number density is changed, modulating the radio wave of the pulsar along the LOS. We analyze the measurements of DM and rotation measure (RM) to determine the variation in the environment over the 110 minute observation. In this work, we dedisperse the raw data in the frequency time of 2 minutes integration in a series of DM trials to obtain the pulse profiles. Then we calculate each profile's signal-to-noise ratio (SNR) based on each DM trial and determine the best DM as the one with the highest SNR in the profile. Figure 2(a) shows the variation in the measured DM in a short duration of 2 minutes, showing that a large increase in DM up to 0.05 pc cm^{-3} is detected in the event. This detection implies that a compact plasma environment appears along the LOS. Moreover, the changes in the

measured DM result in an additional delay in the pulsar timing of about $130 \mu\text{s}$ at the frequency of 1250 MHz.

To estimate the averaged parallel magnetic field along the LOS during the DM jumps, the RM of pulsar B1929+10 is determined over the entire 110 minute observation. The RM was measured using the LAPUDA software package.⁹ We consider the diffusion in the Stokes (Q , U) space for each phase bin. Then, we fit the relation between the polarization position angle and the square of the wavelength, λ^2 . In Figure 2(b), one can see that there is a decreasing trend (the gray line; $\text{RM} = -3.0 \times 10^{-4}t - 5.96$, where RM and t are measured in units of rad m^{-2} and seconds, respectively) in the measured RM. We utilize the ionFR software package¹⁰ to estimate the contribution of the Earth's ionosphere, RM_{ion} , to the RM. We find that the RM_{ion} has no change during our 110 minute observation. This suggests that the decrease with a linear trend in the measured RM throughout the 110 minutes has another origin. Besides, a significant increase up to 0.7 rad m^{-2} in RM is detected during the DM jumps. Consider the relation

⁹ <https://github.com/lujig/lapuda>

¹⁰ <https://github.com/csobey/ionFR>

$RM \propto \int n_e B_z dl$, where B_z corresponds to the field component parallel to the LOS. Taking the variations in both the DM and the RM into account, we can estimate the average parallel magnetic field along the LOS, $\langle B_z \rangle = 12.3 \mu\text{G} (\Delta\text{RM}/0.1 \text{ rad m}^{-2}) / (\Delta\text{DM}/0.01 \text{ pc cm}^{-3}) = 17.22 \mu\text{G}$, up to 17 times the strength of the Galactic magnetic field (for the Galaxy, $\langle B_z \rangle \sim 1 \mu\text{G}$; see D. R. Lorimer & M. Kramer 2012) in the event. It suggests the presence of a magnetized environment with a highly compact plasma, which modulates the flux density of pulsar B1929+10 by a magnitude of 3 orders and causes changes in the measured DM and RM. Figure 2(a) also shows that the DM has a ramp with a positive slope variation before the event.

The frequency-dependent (chromatic) DM is a stochastic component that is worth studying because the chromatic dispersion can influence radio-wave propagation and yield an additional delay in the pulsar timing (e.g., J. M. Cordes et al. 2016; M. T. Lam et al. 2020). To determine whether the event is affected by the chromatic dispersion, we quantify the total dispersive delay that includes the contributions of all possible DM components. Following J. M. Cordes et al. (2016), we consider the chromatic DM as a power-law function of the frequency f (i.e., $\propto f^\beta$). The total dispersive delay resulting in the time difference between frequencies can be described as

$$\Delta t = \mathcal{D} \times \kappa_{\text{DM}} \times \left(\frac{1}{f_1^\alpha} - \frac{1}{f_2^\alpha} \right), \quad (2)$$

where κ_{DM} denotes the total DM that includes all possible components. κ_{DM} corresponds to the DM component described in Equation (1) if α is reduced to 2, while α is a mixed index that describes the relation between the total dispersive effect and frequency.

We dedisperse the raw data in the frequency time of 2 minutes integration into a range of κ_{DM} and α trials to get the pulse profiles. We calculate the SNR of the pulse profile of each κ_{DM} and α trial based on the peak and the fluctuation in the ‘‘pulse-off’’ of the pulse profile, similar to the pdmp software package (W. van Straten & M. Bailes 2011) that is used to search a specified range of barycentric period and DM of the pulsar. We consider the SNR as a function of the κ_{DM} and α and search the optimal values for κ_{DM} and α according to the highest SNR in the $(\kappa_{\text{DM}}-\alpha)$ plane. Then we determine the best κ_{DM} and α and use them to dedisperse the raw data of all Stokes parameters (I , Q , U , V) in a 2 minute integration in the frequency-time domain. Figures 2(c) and (d) show the measurement of the chromatic DM in this observation, implying that there is no significant effect of the chromatic dispersion on the radio-wave propagation of pulsar B1929+10. It is worth noticing that there is a slight deviation from 2 in the value of α detected after the observation time of 2000 s, particularly in the range of 5000–6200 s. This deviation is due to system noise and cannot be considered as evidence for the effect of chromatic dispersion.

3.3. Measurement of the Narrowband Pulsar Timing

The time of arrival of the radio waves is not only used to detect nanohertz GWs directly but also is believed to be a probe to reveal the environment along the LOS (e.g., J. M. Cordes et al. 1986; J. W. Armstrong et al. 1995; N. D. R. Bhat et al. 2004; K. Liu et al. 2014). The event shows an extreme fluctuation, decreasing in flux density by 3 orders of

magnitude, encouraging us to analyze the pulse arrival time of pulsar B1929+10 in this observation. As Figure 1 shows, the characteristics of fluctuations in observed flux density display frequency differences, implying that radio waves of different frequencies are differently affected by the environment of the ISM. To accurately detect the properties of radio waves propagating in multifrequency paths, we analyze the narrowband timing of pulsar B1929+10.

Figure 3 shows the timing residuals of pulsar B1929+10. It demonstrates that the radio waves have a significant time delay in the event. These timing residuals depend on the observing frequencies. The residual timing of the radio waves at the two lower frequencies (1100 and 1050 MHz) has maximum values with an average of 300 μs . The arrival time of the pulse display decreased feature with the frequency increased, implying that the pulsar timing behavior of pulsar B1929+10 can be interpreted as the DM increase. The result in Figure 2(a) shows a change in the measured DM of up to 0.05 pc cm^{-3} in the event. This increase can introduce a delay of about 130 μs into the pulsar timing at 1250 MHz. These results suggest that the radio waves of pulsar B1929+10 are affected by the environment, which is characterized by compact electron density along the LOS. In Figure 4, one can see the highly corrected points between the adjacent frequency pairs (i.e., between 1100 and 1050 MHz). This suggests that the timing measurements are caused by the DM increase. However, the correlation between pairs of frequencies below 1200 MHz and those beyond 1200 MHz does not show significant decreases as the frequency bands increase, implying that some other effects influence the timing measurements, such as the changes in pulse shape or the process of refraction. It is worth noticing that at a large delay, the correlations diverge. This is because the radio emission flux at a frequency lower than 1200 MHz decreases on the order of 3 in the event, resulting in large errors in timing measurements.

3.4. Pulse Shape

To detect the pulsar timing behavior affected by the changes in the pulse shape, we analyze the profile in 2 minutes of integration throughout the 110 minute observation. We define the average pulse phase ϕ_0 to detect the change of the profile,

$$\tan \phi_0 = \frac{[\sin \phi \cdot I(\phi)]}{[\cos \phi \cdot I(\phi)]}, \quad (3)$$

where ϕ and $I(\phi)$ correspond to the pulse phase with a range of $0-2\pi$ and flux density, respectively. To accurately detect the variation of the pulse shape intrinsic to pulsar B1929+10, we further define the standard deviation of the pulse phase σ_ϕ , the skewness of the pulse phase S_ϕ , and the kurtosis of the pulse phase K_ϕ as follows:

$$\sigma_\phi = \sqrt{\frac{\sum_\phi \frac{[\cos(\phi - \phi_0) + 1]^4}{16} \cdot I(\phi) \cdot (\phi - \phi_0)^2}{\sum_\phi I(\phi)}}, \quad (4)$$

$$S_\phi = \frac{1}{\sigma_\phi} \left(\frac{\sum_\phi \frac{[\cos(\phi - \phi_0) + 1]^4}{16} \cdot I(\phi) \cdot (\phi - \phi_0)^3}{\sum_\phi I(\phi)} \right)^{\frac{1}{3}}, \quad (5)$$

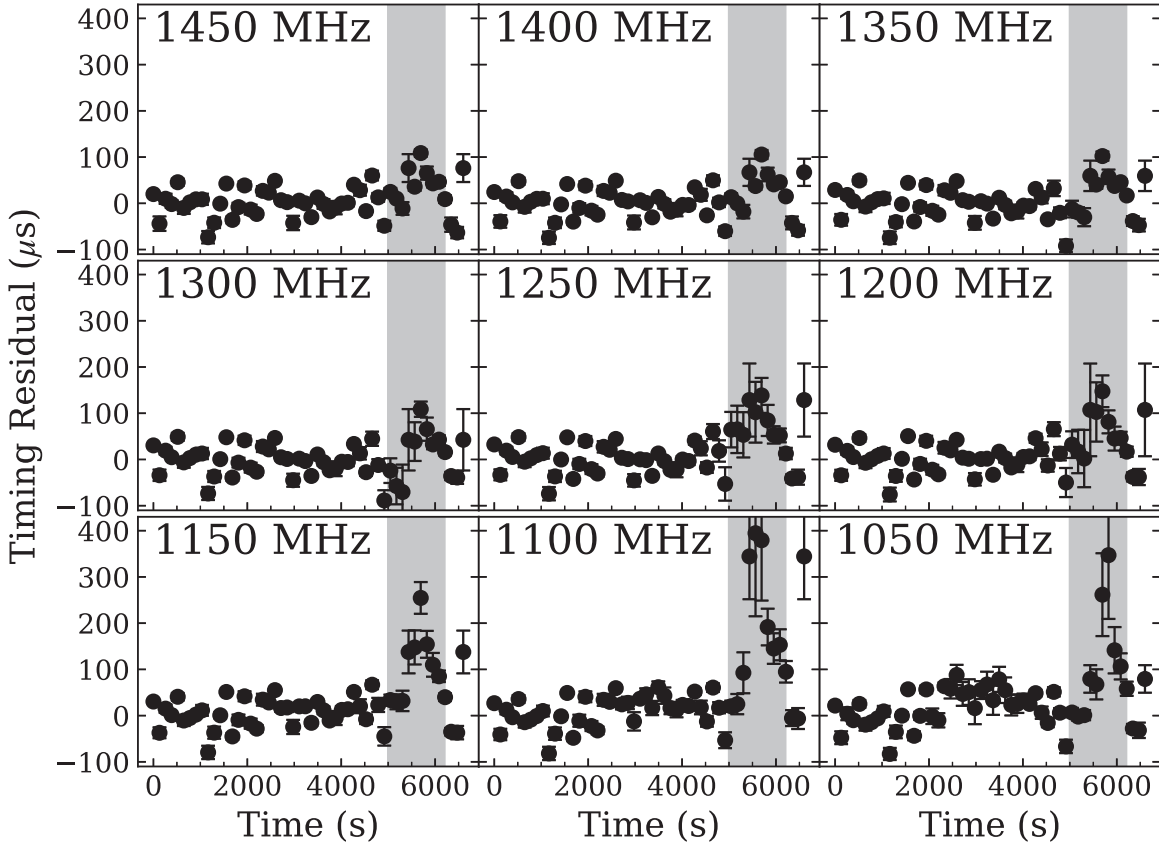


Figure 3. Narrowband pulsar timing of nine narrow frequencies with a bandwidth of 50 MHz as a function of the observation time for pulsar B1929+10; their corresponding frequencies are included in the upper left corner of each panel, as labeled. In each panel, the black dot represents the arrival time of a pulse profile in a short duration of 2 minutes.

$$K_\phi = \frac{1}{\sigma_\phi} \left(\frac{\sum_\phi \frac{[\cos(\phi - \phi_0) + 1]^4}{16} \cdot I(\phi) \cdot (\phi - \phi_0)^4}{\sum_\phi I(\phi)} \right)^{\frac{1}{4}}. \quad (6)$$

Here ϕ_0 denotes the average pulse phase, and $\frac{[\cos(\phi - \phi_0) + 1]^4}{16}$ corresponds to the window function.

Figure 5 shows the measured values of ϕ_0 , σ_ϕ , S_ϕ , and K_ϕ over the entire 110 minute observation. For the results of the bandwidth of 450 MHz, one can see that there are no variations in ϕ_0 and σ_ϕ . Slight increases in S_ϕ and K_ϕ are detected in the event. The slight changes of S_ϕ and K_ϕ may be caused by the effect of the system response since the flux density is decreased with an amplitude of 10^{-3} . These results suggest that there are no significant variations in pulse shape for the bandwidth of 450 MHz over the entire 110 minute observation. However, for the results at a frequency lower than 1200 MHz, significant increases in all of the parameters ϕ_0 , σ_ϕ , S_ϕ , and K_ϕ are detected in the event. The change of ϕ_0 is up to 0.6° . This increase in ϕ_0 corresponds to the delay of $370 \mu\text{s}$ for pulsar B1929+10. This detection provides strong evidence that the pulse shape of the profile at a frequency lower than 1200 MHz has changed. Consequently, the pulsar timing behavior shown in Figure 3 can be attributed to both the DM increase and the changes in the pulse shape effects.

The parameter S_ϕ is used to distinguish the effect of the chromatic dispersion and scattering on the radio-wave propagation of pulsar B1929+10. If the radio waves from pulsar B1929+10 are affected by the scattering effect, S_ϕ would have changed. The chromatic dispersion impacts on the

radio waves of the pulsar yield an effect that can be regarded as the convolution between the radio waves and rectangular function. On the contrary, the scattering impact on the radio-wave propagation can be equivalent to the convolution of the radio waves and a power-law function (e.g., J. M. Cordes et al. 2006). These properties can be distinguished by S_ϕ because the result due to the convolution of a rectangular function cannot change the skewness feature of the samples. On the contrary, the effect owing to the scattering can alter the value of S_ϕ . Figure 5 shows an S_ϕ change. This result indirectly implies that the scattering effect still impacts the radio-wave propagation of pulsar B1929+10 in the event. This result is consistent with detecting the weak chromatic dispersion effect shown in Figures 2(c) and (d).

4. Origin of the Event

4.1. The Outflows near the Pulsar

Based on the detection of the plasma lensing events due to the ESEs in previous observations (e.g., R. L. Fiedler et al. 1987; I. Cognard et al. 1993; K. W. Bannister et al. 2016), these events are significantly different from the variations observed in pulsar B1929+10. As shown in Figure 1, the observed flux density at a frequency lower than 1375 MHz has a decrease of up to 3 orders, and at certain frequencies, the decrease exceeds 3 orders of magnitude during the observation range of 5000–6200 s. Meanwhile, the variations in flux density of pulsar B1929+10 are seen here as frequency dependence. For those frequencies whose flux densities show the “valley” structure, the arrival times of the bottom of the

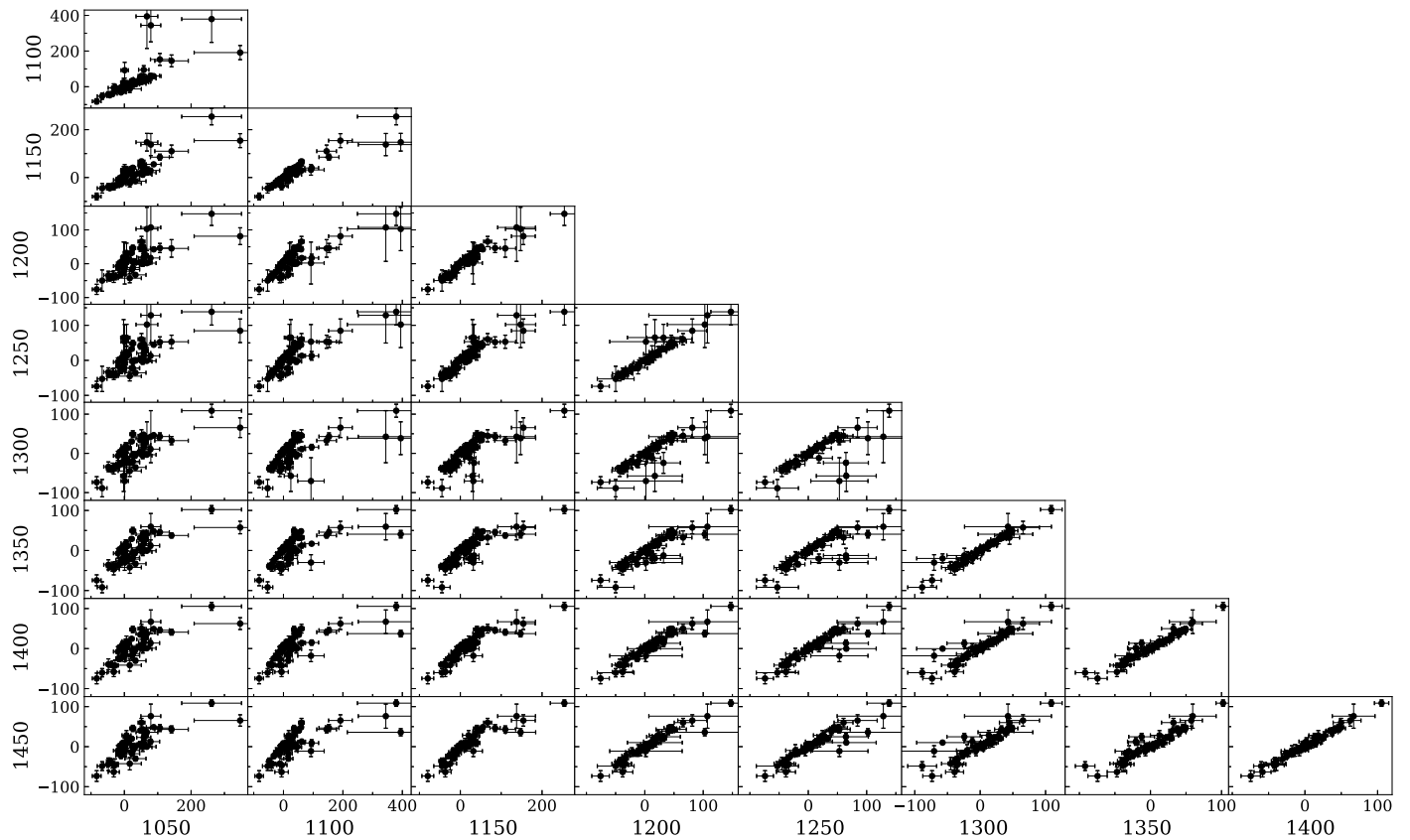


Figure 4. The scatter plots of the timing residuals between pairs of frequencies. The frequencies are labeled and in units of MHz. The dots correspond to the arrival times of pulse profiles in a short duration of 2 minutes and are in units of microseconds.

“valley” structure have increased with the decreased frequency (see Figure 1(b)). These behaviors are hardly interpreted as the plasma lensing events caused by the ESEs.

The X-ray studies of a bow shock structure around pulsar B1929+10 imply that there exists an axial outflow that is opposite to its proper motion. This axial outflow appears to be longer than $4'$ (e.g., Q. D. Wang et al. 1993; W. Becker et al. 2006; S. I. Kim et al. 2020; S. K. Ocker et al. 2024). Moreover, deep X-ray spectral imaging was carried out by S. I. Kim et al. (2020), revealing two new lateral outflows around this pulsar. The outflows eclipse the radio wave of pulsar B1929+10, resulting in variations in this pulsar, such as the flux density having an extreme decrease up to 10^{-3} and changes in the pulsar timing. In addition, the outflows can bend the rays, causing the plasma lensing process to increase the flux density, which is significant at 1050 MHz during the range of 2000–4000 s. The variation in ΔDM of approximately 0.05 pc cm^{-3} detected in the event can help us constrain the region responsible for the plasma lensing. According to Equation (7) in J. M. Cordes et al. (2017), this increase yields that the focal distance d_f is less than 1 pc. The value of d_f is evidence of the region of the plasma lensing close to pulsar B1929+10. Furthermore, the region near the pulsar could be larger, resulting in a short timescale and yielding a larger focal distance. A schematic diagram of the eclipse and bending process is shown in Figure 6(a); the outflows eclipse and bend the rays of pulsar B1929+10 and then result in the radiative behavior of pulsar B1929+10 within the short timescale (about 20 minutes) seen in this observation. To be sure, the physical origin of the outflows is unclear, but it might not be surprising

for active astrophysical objects, as in the case of solar energetic particle events (K. Whitman et al. 2023).

The variations in the flux density of pulsar B1929+10 can help us further estimate the outflows’ parameters. As Figure 1 shows, the flux density decreases by 3 orders of magnitude, and the maximum timescale of the modulation is detected at 1250 MHz. If we consider that our observation frequency is near the plasma frequency ν_p (i.e., $\nu_p \approx 1250 \text{ MHz}$), then according to the relation $\nu_p = \sqrt{\frac{e^2 n_e}{\pi m_e}}$ (D. R. Lorimer & M. Kramer 2012), the electron number density is up to $2 \times 10^{10} \text{ cm}^{-3}$. This electron density and the increase in ΔDM can estimate that the outflows have a size of approximately 77 km. Assuming that the outflows consist of electrons and protons, and the emission altitude of the normal radio pulsars is about 1000 km, the mass of the outflows is up to about $250 \times 10^3 \text{ kg}$. The outflow just ejects from this pulsar since an extremely high electron number density cannot last long in the ISM. However, the increase of ΔRM is about 0.7 rad m^{-2} in the event, which indicates a low magnetic field. It is challenging to understand the highly dense outflow that only has a low magnetic field. Besides, the low magnetic field speculated from $\Delta RM/\Delta DM$ is typical for pulsar wind nebulae that are characteristic with low magnetization (e.g., S. P. Reynolds et al. 2017). But by now we have no idea on whether the blocking particles are relativistic or not.

The electron number density of the outflows could also be estimated by assuming a major absorption/scattering mechanism that causes the optical depth τ . The mechanism should be manifestly more effective at low frequency than at high frequency, as shown in Figure 1, so typical scattering processes

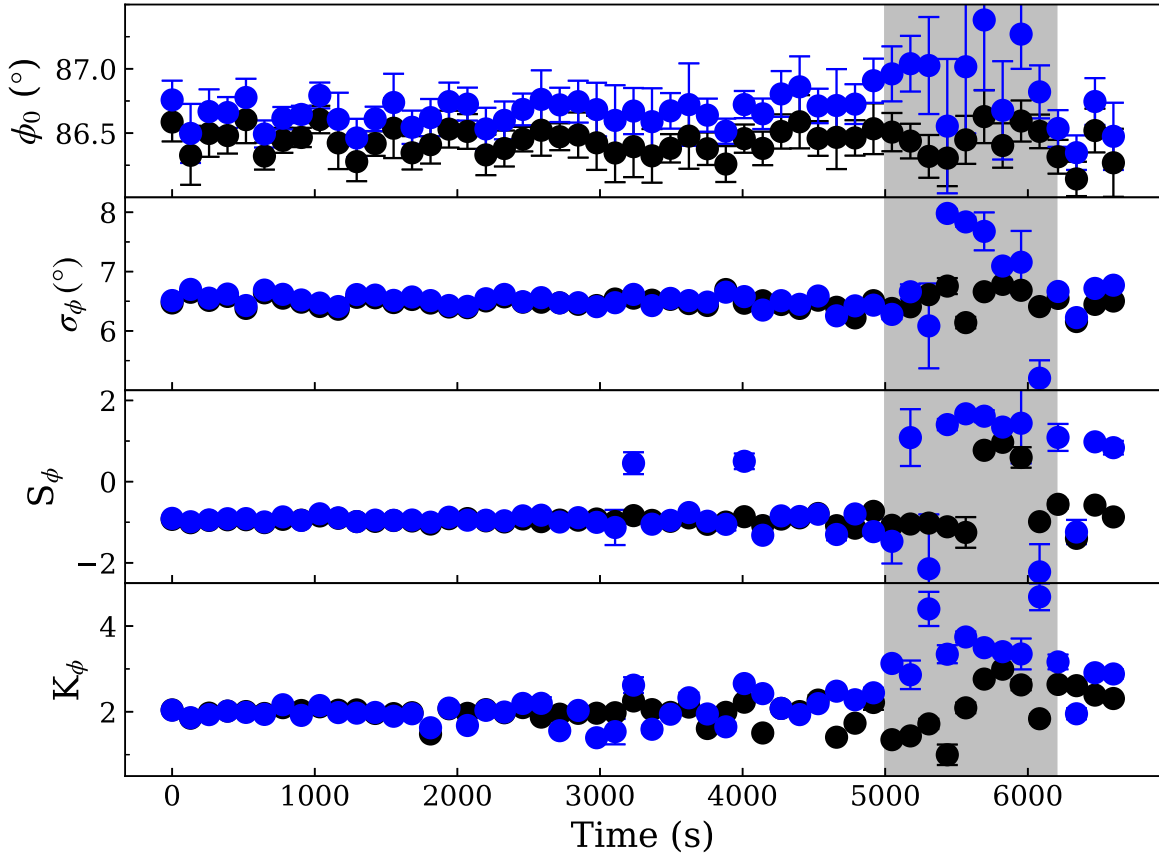


Figure 5. The parameters are used to detect the behaviors of the profile defined in Equations (3), (4), (5), and (6) as a function of the observation time. The black dots represent the results of the observing frequency 1250 MHz with a bandwidth of 450 MHz, while the blue dots correspond to that of the frequencies that are lower than 1200 MHz. The dots correspond to the results in a 2 minute integration. The vertical gray shadow corresponds to the region of the event.

should be ruled out. Besides, the small RM variation corresponds to the low magnetic field, so absorption mechanisms related to the magnetic field (cyclotron/synchrotron absorption) are less favored. We consider bremsstrahlung absorption (free-free absorption) as the major absorption mechanism, which is typical for astrophysical plasmas (V. V. Zheleznyakov 1996). The absorption coefficient of bremsstrahlung absorption at frequency ν for electromagnetic waves is (V. V. Zheleznyakov 1996)

$$\alpha_{\text{em},\nu}^{\text{ff}} = \frac{\nu_p^2 \nu_{\text{eff}}}{\nu^2 c \sqrt{1 - \nu_p^2/\nu^2}}, \quad (7)$$

where $\nu_p = \sqrt{4\pi n_e e^2/m_e}/2\pi$ is the plasma frequency and ν_{eff} is the collision frequency that depends on the electron number density n_e , temperature T , etc. To give some constraints on the blocking flow's parameters, we try to fit the maximum optical depths of the nine frequency bands with an optical depth function $\tau_{\text{em},\nu}^{\text{ff}} = \alpha_{\text{em},\nu}^{\text{ff}} l$ assuming a uniform electron distribution. The least-squares fitting result is shown in Figure 6(b). The plasma frequency derived is close to the observing frequency, and the electron density is about 10^9 – 10^{10} cm^{-3} .

4.2. Plasma Lensing

Usually, flux modulation on timescales of minutes to hours is attributed to interstellar scintillation, i.e., radio-wave deflection by the ISM and interference of the scattered light. This particular observation is special because there is a large-

amplitude modulation with a broad frequency bandwidth on a relatively large timescale of ~ 100 minutes at 1 GHz, and the minimum radio flux is about 10^{-3} of the average flux. This could be interpreted in terms of plasma lensing if the main image of the pulsar is broken into a small number of images of comparable brightnesses and small angular separations.

As an order-of-magnitude estimation, let us consider a simplified picture of the interference pattern created by two images separated by a on the lens plane, with a matching the lens size. Then, the width of the fringe pattern created on the observer's plane is

$$\begin{aligned} \lambda D_1/a &\sim 0.3 \text{ m} \times 0.331 \text{ kpc}(1-s)/a \sim 3 \\ &\times 10^{22} \text{ cm}^2(1-s)/a, \end{aligned} \quad (8)$$

where λ is the wavelength, D_p is the pulsar distance, the lens distance $D_1 = D_p(1-s)$, and s is the fractional distance between the pulsar and the lens; we have taken $D_p = 0.331 \text{ kpc}$ (e.g., W. F. Brisken et al. 2002).

Taking the reference frame of a static pulsar-lens LOS, the relative velocity between the observer and this LOS is $\mathbf{v} = (1-s)/s \mathbf{V}_p + \mathbf{V}_{\text{Earth}}$. At the time of this observation, $V_{\text{Earth,ra}} = -18.3 \text{ km s}^{-1}$, and $V_{\text{Earth,dec}} = 10.4 \text{ km s}^{-1}$, whereas $V_{p,ra} = -183.3 \text{ km s}^{-1}$, and $V_{p,dec} = 63.2 \text{ km s}^{-1}$. Thus, the amplitude of the relative velocity is $v = 165\sqrt{s^2 - 0.72s + 1.23/s} \text{ km s}^{-1}$. Assuming the angle between the modulation direction of the fringe pattern and \mathbf{v} is α , then the width of the fringe pattern on a $\Delta t = 100$ minute

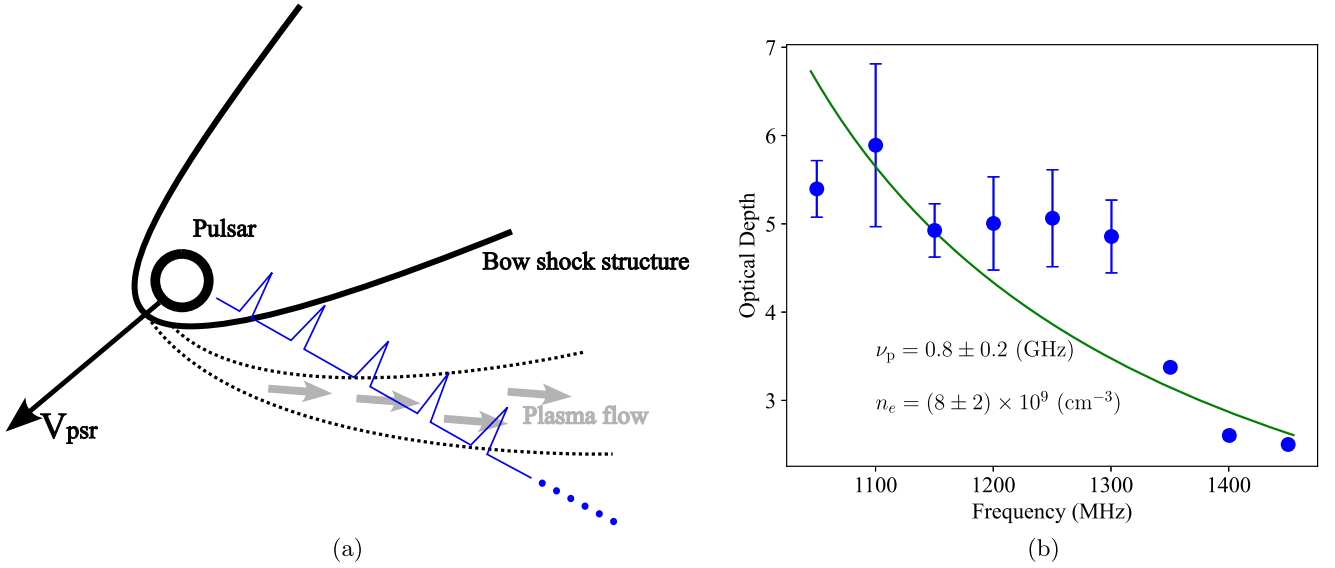


Figure 6. (a) Sketch for the outflow from the pulsar. To better unravel the local environment near the pulsar, the bow shock structure and the proper motion are also included. (b) Fitting of optical depths under nine frequency bands using bremsstrahlung absorption. The optical depths are estimated from Figure 1 through $\tau = \ln(I/I_{\text{min}})$ and are shown as blue dots with error bars in the plot. The errors are estimated from the fluctuation in flux density in the “pulse-off” regions. The green curve of $\tau_{\text{cm},\nu}^{\text{ff}}$ is derived from the least-squares fitting. The derived ν_p and n_e are also marked on the plot.

scale is

$$v\Delta t \cos \alpha \sim \cos \alpha \sqrt{s^2 - 0.72s + 1.23} / s \times 10^{11} \text{ cm.} \quad (9)$$

Combining these two expressions, we get

$$a \sim \frac{3 \times 10^{11}}{\cos \alpha} \frac{s(1-s)}{\sqrt{s^2 - 0.72s + 1.23}} \text{ cm} \sim 3 \times 10^{11} \frac{s(1-s)}{\cos \alpha} \text{ cm.} \quad (10)$$

This corresponds to a sub-au scale length unless the relative velocity is almost perfectly perpendicular to the fringe pattern.

If the DM increment is due to the plasma lens creating the fringe pattern, then the implied electron density enhancement in the lens,

$$\Delta n_e = \Delta \text{DM} / a / A \sim 0.05 \cos \alpha / A \text{ pc cm}^{-3} / (3s(1-s) \times 10^{11} \text{ cm}) \times \sim 5 \times 10^5 \frac{\cos \alpha}{As(1-s)} \text{ cm}^{-3}, \quad (11)$$

is very high unless the aspect ratio A of the lens (the ratio of its LOS to transverse scales) is very large. Such a small size and high density are not typical of the ISM and are possibly connected to the pulsar wind.

We have considered the additional conditions $\kappa > 1$ and $\kappa \tilde{\nu} > 1$ for plasma lensing to be responsible for the large-scale, large-amplitude modulation. Here the lensing convergence κ represents a characteristic dimensionless lens amplitude. The reduced frequency $\tilde{\nu} = (a/r_F)^2$, with r_F being the Fresnel scale, is a normalizing quantity proportional to the observing frequency such that $\kappa \tilde{\nu}$ is the phase shift induced by the lens (e.g., X. Shi & Z. Xu 2021; D. L. Jow et al. 2023). Whereas κ being greater than unity is required for multiple images to exist, $\kappa \tilde{\nu} > 1$ is required so that radio-wave effects do not smear out the flux modulation. However, both conditions can be satisfied at all s values and thus give no constraint on the screen distances.

4.3. An Extra Celestial Object and Other Origins

An extra celestial object with a compact electron density atmosphere (brown dwarf or giant planet) that transversely passes through the LOS to pulsar B1929+10 can also be responsible for this event. Its appearance causes variations in the flux density of this pulsar. Moreover, its atmosphere provides an environment with a magnetized and compact electron density to yield the DM and RM jumps when the radio wave of pulsar B1929+10 passes through it. Figure 1 shows the variations in flux density of this pulsar, which can help us to constrain the celestial object that has a diameter of about 2.4×10^5 km since the flux “valley” structure (the radio emission modulated by the celestial object) only lasts approximately 20 minutes. Here we consider the velocity dispersion estimated with the virial theorem near the solar system to be approximately 200 km s^{-1} . This celestial object can be additionally verified through optical observations. Unfortunately, R. P. Mignani et al. (2002) reported the optical observation of pulsar B1929+10 and found that this pulsar has optical emission behavior. In addition, we have tried to find a star near our LOS to pulsar B1929+10. According to the VizieR Catalogue Collection,¹¹ the minimum angular distance from the observed stars to pulsar B1929+10 is $1''.896$, corresponding to a Gaia source¹² (Gaia Collaboration 2022) but a lack of distance measurements. Besides, the small RM variation is still a problem.

It is still worth noticing the possibility of the solar elongation of this pulsar at the time of our observation. It could be another possibility that is responsible for the radiative behaviors of pulsar B1929+10. Figures 2(a) and (b) show that changes in both the DM and RM were detected before the event. These phenomena also indicate that this pulsar's motion through its local environment can account for some of the changes.

¹¹ <https://vizier.cds.unistra.fr/viz-bin/VizieR>

¹² id: 4314712501956058752.

5. Conclusions

As Figure 1 shows, the variations in the radio emission flux of pulsar B1929+10 show a frequency difference. Only frequencies below 1375 MHz show the radio emission behavior with a “valley” structure in the flux. The variations in the flux density at frequencies below 1150 MHz (the yellow patches with a positive slope in Figure 1(a)), especially at 1050 MHz, show that the observed flux density is reduced by a factor of 10 during the observation range of 2000–4000 s and could be interpreted as the plasma lensing event. Moreover, the event shows that the flux density is modulated by a decrease of 3 orders of magnitude forming a “valley” structure within a rapid timescale of about 20 minutes; this modulation is first detected in the radio emission behaviors of the pulsars.

Figures 2(a) and (b) show that both the DM and the RM experience a jump during the event, indicating an environment that causes a decrease in flux density and an increase in electron density. The DM increase can cause an additional increase in RM. For pulsar B1929+10, the 0.05 pc cm^{-3} increase yields an RM increase of 0.2 rad m^{-2} . This RM increase due to the DM increase is 0.2 rad m^{-2} lower than the measured RM increase up to 0.7 rad m^{-2} . This deviation implies an additional magnetized environment, which modulates the magnetic field component parallel to the LOS of pulsar B1929+10. Moreover, the increase in RM in the event is positive. That is the opposite of the negative ramp in RM and the positive ramp in DM before the event. The radio emission behavior detected here can be useful for directly detecting chromatic DM. Following J. M. Cordes et al. (2016), we investigate the effect of the chromatic dispersion and analyze the behavior of the radio waves of pulsar B1929+10. Figures 2(c) and (d) show the detection of the chromatic DM. Variations in the index α and chromatic DM are detected after the observation time of 2000 s, but these increases may be due to the narrowband frequency introducing correlation noise into the data and the system noise, and they are weak evidence for the detection of the chromatic DM.

Pulse times of arrival of the pulsars are believed to be a probe to detect weak GWs with high-precision timing since the GW can introduce a systematic time delay into the pulsar timing measurement (e.g., J. H. Taylor & J. M. Weisberg 1989; M. Kramer et al. 2006; G. Agazie et al. 2023; EPTA Collaboration et al. 2023; H. Xu et al. 2023). We analyze the pulse’s arrival time at pulsar B1929+10 to understand whether the radio waves are affected by the flux density event. Figure 3 shows the pulsar timing results for the narrow band. It implies that a significant time delay is detected in the event, consistent with a dispersive delay caused by the increase in DM of up to 0.05 pc cm^{-3} . These results provide strong evidence of a significant environmental change along the LOS of pulsar B1929+10. The behavior of the pulse shape shown in Figure 5 indicates that the pulsar timing behavior of pulsar B1929+10 can also be attributed to the changes in pulse shape in the event.







There are three outflows around this pulsar that were observed (e.g., S. I. Kim et al. 2020). As Figure 6(a) shows, the outflows eclipse the radio waves of pulsar B1929+10 and bend its ray, yielding the plasma lensing effect that can be responsible for the above variations in pulsar B1929+10. The outflow may be just from this pulsar since it has a high electron number density up to 10^{10} cm^{-3} (the result is estimated from the variations in the flux density or the bremsstrahlung absorption). However, the outflow with a low

magnetic field of approximately $17 \mu\text{G}$ is still a challenge. In addition, as discussed in Section 4.3, an extra celestial object that transverse passes through the LOS to pulsar B1929+10 in the event is still possible. Its appearance could account for the detection of most of the variations. Also, a nonlensing physical process is possible; for example, this pulsar’s motion through its local environment can contribute to some of the changes. Moreover, the effect of the solar system, such as that related to the variation of the pulsar’s solar elongation, cannot be completely ruled out.

Acknowledgments

This work is supported by the Strategic Priority Research Program of the Chinese Academy of Sciences (Nos. XDA0350501, XDB0550300), the National SKA Program of China (No. 2020SKA0120100), the National Natural Science Foundation of China (12133003), the Guangxi Talent Program (Highland of Innovation Talents), the Major Science and Technology Program of Xinjiang Uygur Autonomous Region, grant No. 2022A03013-2, the Guizhou Provincial Science and Technology Projects (QKHFQ[2023]003, QKHPTRC-ZDSYS [2023]003, QKHFQ[2024]001-1), and the National Key R&D Program of China No. 2022YFC2205202. We are greatly indebted to Prof. James M. Cordes for carefully reading the manuscript and for his insights about radio waves traveling in the interstellar medium. We would also like to thank Kejia Lee, Junzhi Wang, Haozhu Fu, and Xinyu Zhu for their useful discussions. This work made use of the data from the Five-hundred-meter Aperture Spherical radio Telescope (FAST), operated by the National Astronomical Observatories, Chinese Academy of Sciences.

ORCID iDs

Zhengli Wang  <https://orcid.org/0000-0002-8839-9778>
 Shunshun Cao  <https://orcid.org/0009-0007-3817-8188>
 Yulan Liu  <https://orcid.org/0000-0001-9986-9360>
 Xun Shi  <https://orcid.org/0000-0003-2076-4510>
 Jinchen Jiang  <https://orcid.org/0000-0002-6465-0091>
 Enwei Liang  <https://orcid.org/0000-0002-7044-733X>
 Weiyang Wang  <https://orcid.org/0000-0001-9036-8543>
 Heng Xu  <https://orcid.org/0000-0002-5031-8098>
 Renxin Xu  <https://orcid.org/0000-0002-9042-3044>

References

- Agazie, G., Anumarlapudi, A., Archibald, A. M., et al. 2023, *ApJL*, 951, L8
 Armstrong, J. W., Rickett, B. J., & Spangler, S. R. 1995, *ApJ*, 443, 209
 Bannister, K. W., Stevens, J., Tuntsov, A. V., et al. 2016, *Sci*, 351, 354
 Becker, W., Kramer, M., Jessner, A., et al. 2006, *ApJ*, 645, 1421
 Bhat, N. D. R., Cordes, J. M., Camilo, F., Nice, D. J., & Lorimer, D. R. 2004, *ApJ*, 605, 759
 Briskin, W. F., Benson, J. M., Goss, W. M., & Thorsett, S. E. 2002, *ApJ*, 571, 906
 Cimò, G., Beckert, T., Krichbaum, T. P., et al. 2002, *PASA*, 19, 10
 Cognard, I., Bourgois, G., Lestrade, J.-F., et al. 1993, *Natur*, 366, 320
 Cordes, J. M., Pidwerbetsky, A., & Lovelace, R. V. E. 1986, *ApJ*, 310, 737
 Cordes, J. M., Rickett, B. J., Stinebring, D. R., & Coles, W. A. 2006, *ApJ*, 637, 346
 Cordes, J. M., & Shannon, R. M. 2010, arXiv:1010.3785
 Cordes, J. M., Shannon, R. M., & Stinebring, D. R. 2016, *ApJ*, 817, 16
 Cordes, J. M., Wasserman, I., Hessels, J. W. T., et al. 2017, *ApJ*, 842, 35
 Demorest, P. B., Ferdman, R. D., Gonzalez, M. E., et al. 2013, *ApJ*, 762, 94
 EPTA Collaboration/PTA Collaboration, Antoniadis, J., et al. 2023, *A&A*, 678, A50
 Er, X., & Mao, S. 2022, *MNRAS*, 516, 2218

- Fiedler, R. L., Dennison, B., Johnston, K. J., & Hewish, A. 1987, *Natur*, **326**, 675
- Foster, R. S., & Backer, D. C. 1990, *ApJ*, **361**, 300
- Foster, R. S., & Cordes, J. M. 1990, *ApJ*, **364**, 123
- Gaia Collaboration 2022, *yCat*, **I/355**
- Hobbs, G., Lyne, A. G., Kramer, M., Martin, C. E., & Jordan, C. 2004, *MNRAS*, **353**, 1311
- Hotan, A. W., van Straten, W., & Manchester, R. N. 2004, *PASA*, **21**, 302
- Jiang, P., Tang, N.-Y., Hou, L.-G., et al. 2020, *RAA*, **20**, 064
- Jiang, P., Yue, Y., Gan, H., et al. 2019, *SCPMA*, **62**, 959502
- Jow, D. L., Pen, U.-L., & Feldbrugge, J. 2023, *MNRAS*, **525**, 2107
- Kim, S. I., Hui, C. Y., Lee, J., et al. 2020, *A&A*, **637**, L7
- Kramer, M., Stairs, I. H., Manchester, R. N., et al. 2006, *Sci*, **314**, 97
- Kramer, M., Stairs, I. H., Manchester, R. N., et al. 2021, *PhRvX*, **11**, 041050
- Lam, M. T., Lazio, T. J. W., Dolch, T., et al. 2020, *ApJ*, **892**, 89
- Liu, K., Desvignes, G., Cognard, I., et al. 2014, *MNRAS*, **443**, 3752
- Liu, Y., Verbiest, J. P. W., Main, R. A., et al. 2022, *A&A*, **664**, A116
- Lorimer, D. R., & Kramer, M. 2012, *Handbook of Pulsar Astronomy* (Cambridge: Cambridge Univ. Press)
- Main, R., Yang, I. S., Chan, V., et al. 2018, *Natur*, **557**, 522
- Men, Y., & Barr, E. 2024, *A&A*, **683**, A183
- Mignani, R. P., De Luca, A., Caraveo, P. A., & Becker, W. 2002, *ApJL*, **580**, L147
- Ocker, S. K., Cordes, J. M., Chatterjee, S., et al. 2024, *MNRAS*, **527**, 7568
- Phillips, J. A. 1990, *ApJL*, **361**, L57
- Rankin, J. M., & Rathnasree, N. 1997, *JApA*, **18**, 91
- Reynolds, S. P., Pavlov, G. G., Kargaltsev, O., et al. 2017, *SSRv*, **207**, 175
- Rickett, B. J. 1990, *ARA&A*, **28**, 561
- Shi, X., & Xu, Z. 2021, *MNRAS*, **506**, 6039
- Taylor, J. H., & Weisberg, J. M. 1989, *ApJ*, **345**, 434
- van Straten, W., & Bailes, M. 2011, *PASA*, **28**, 1
- Wang, Q. D., Li, Z.-Y., & Begelman, M. C. 1993, *Natur*, **364**, 127
- Whitman, K., Egeland, R., Richardson, I. G., et al. 2023, *AdSpR*, **72**, 5161
- Xu, H., Chen, S., Guo, Y., et al. 2023, *RAA*, **23**, 075024
- Zheleznyakov, V. V. 1996, *Radiation in Astrophysical Plasmas*, *Astrophysics & Space Science Library*, Vol. 204 (Berlin: Springer)